

DenseVLM: A Retrieval and Decoupled Alignment Framework for Open-Vocabulary Dense Prediction

Yunheng Li¹, Yuxuan Li¹, Quansheng Zeng¹, Wenhui Wang^{3,4}, Qibin Hou^{1,2,†}, Ming-Ming Cheng^{1,2}

¹ VCIP Lab, Computer Science, NKU ²NKIARI, Futian, Shenzhen

³OpenGVLab, Shanghai AI Laboratory ⁴The Chinese University of Hong Kong

yunhengli@mail.nankai.edu.cn, yuxuan.li.17@ucl.ac.uk

Abstract

Pre-trained vision-language models (VLMs), such as CLIP, have demonstrated impressive zero-shot recognition capability, but still underperform in dense prediction tasks. Self-distillation recently is emerging as a promising approach for fine-tuning VLMs to better adapt to local regions without requiring extensive annotations. However, previous state-of-the-art approaches often suffer from significant ‘foreground bias’, where models tend to wrongly identify background regions as foreground objects. To alleviate this issue, we propose DenseVLM, a framework designed to learn unbiased region-language alignment from powerful pre-trained VLM representations. By leveraging the pre-trained VLM to retrieve categories for unlabeled regions, DenseVLM effectively decouples the interference between foreground and background region features, ensuring that each region is accurately aligned with its corresponding category. We show that DenseVLM can be seamlessly integrated into open-vocabulary object detection and image segmentation tasks, leading to notable performance improvements. Furthermore, it exhibits promising zero-shot scalability when training on more extensive and diverse datasets.

1. Introduction

Open-vocabulary dense prediction, primarily including object detection [13, 21, 36, 54] and image segmentation [4, 11, 26, 27, 49, 50], aims to identify regions or dense visual concepts of arbitrary categories as described by the text. Benefiting from the powerful pre-trained Vision-Language Models (VLMs), recent open-vocabulary approaches [19, 50, 60] for dense prediction have achieved great progress. These developments highlight the importance of continuing research on VLMs used for dense prediction tasks.

[†]Corresponding Author. Email: houqb@nankai.edu.cn

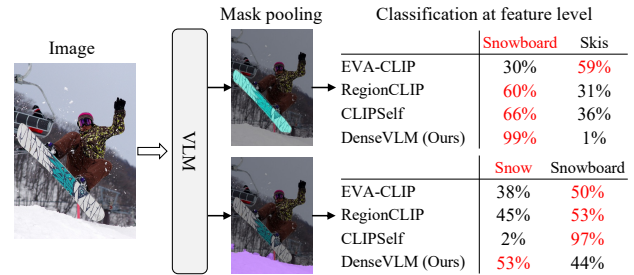


Figure 1. Illustration of foreground bias. Previous methods [41, 46, 57] often produce similar foreground predictions for background regions, our approach effectively alleviates this issue.

Popular VLMs, such as CLIP [39] and EVA-CLIP [41], have exhibited remarkable zero-shot recognition abilities for global image understanding. However, these models expose notable limitations in the understanding of local visual semantics, particularly in localizing and identifying small objects and background stuff [57, 60]. This limitation arises from the training manner of VLMs that align images with global text while neglecting the correspondences between local image regions and text descriptions. To alleviate this issue, some studies train models on region-text or pseudo region-text pairs [25, 30, 56, 57] but they are limited by the high annotation cost and lack scalability for diverse open-world scenes. Alternative self-supervised approaches, such as CLIPSelf [46] and MaskEmbed [5], align region semantics using cropped image representations or reconstruct masked patch embeddings, respectively. These self-distillation approaches, which do not rely on annotated data, offer flexibility and scalability across a variety of datasets.

Despite these advances, previous VLMs [39, 41, 57] pre-trained on image-text and region-text pairs tend to overemphasize the foreground objects at the expense of the background context. This disproportionate focus results in a pronounced predilection for foreground object recognition and causes models to incorrectly associate background regions with foreground labels. Consequently, in dense prediction tasks, these VLMs often misclassify background regions to

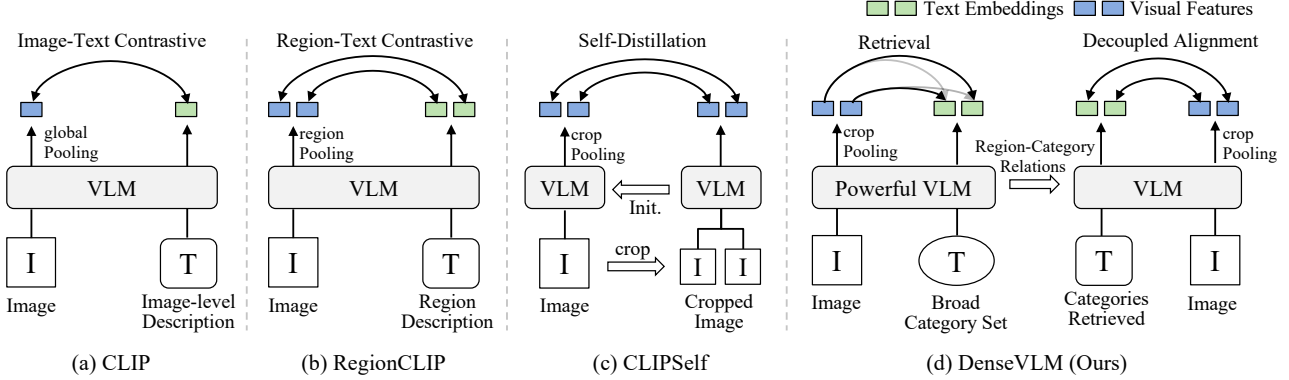


Figure 2. Comparison of different VLMs. Unlike existing methods using (a) image-text contrastive learning [39], (b) region-text contrastive learning [57] or (c) self-distillation [46], our method leverages powerful model representations for region-language alignment.

co-occurring foreground classes—a phenomenon we term as ‘*foreground bias*.’ To clearly illustrate this issue, we present examples that compare the classification results of popular VLMs [41, 46, 57], using ground-truth masks to extract features from the region. As illustrated in Fig. 1, these models tend to confuse ‘snow’ (a background class) with ‘snowboard’ (a foreground object).

To address the challenge of achieving unbiased region-language alignment, we introduce DenseVLM, an effective and general end-to-end framework, as shown in Fig. 2(d). The core idea of DenseVLM is to precisely align unlabeled regions with their corresponding semantic categories. In particular, for unlabeled regions, we leverage a powerful pre-trained VLM with fixed weights to retrieve relevant categories without relying on paired data or self-distillation [41, 46, 57]. To ensure semantic diversity, DenseVLM incorporates a broad and comprehensive set of categories derived from large-scale datasets. A key feature of DenseVLM is its ability to classify regions as either foreground or background based on predefined sets for each category. This classification way enables the decoupling of region features during VLM training, reducing interactions between foreground and background. By decoupling these features, DenseVLM ensures an independent alignment of their respective categories, thus achieving a better region-language alignment. Furthermore, DenseVLM improves both efficiency and performance by directly extracting region features from the dense feature outputs of VLMs, avoiding traditional image cropping [46, 61].

We evaluate the effectiveness of DenseVLM on several open-vocabulary benchmarks [46], including object detection (box classification) and image segmentation (thing and stuff mask recognition). DenseVLM is adaptable to various network architectures, such as ViTs [8] and CNNs [24], and consistently outperforms other competing methods [39, 41, 46]. Furthermore, DenseVLM has great scaling ability, showing promising performance improvement when scaling up the training set based on the SA-1B [20] dataset.

For downstream tasks, DenseVLM improves the two-stage models [21] of OV-COCO [2] and OV-LVIS [14] in open-vocabulary object detection and achieves notable gains in open-vocabulary semantic segmentation over state-of-the-art methods such as SAN [50] and Cat-Seg [4]. We summarize our contributions as follows.

- We propose DenseVLM, an effective and general region-language alignment framework that alleviates the common issue of foreground bias.
- DenseVLM leverages a powerful VLM to retrieve labels for unlabeled regions, decouples interference between features of foreground and background regions, and enhances semantic alignment of these regions.
- Extensive experiments on dense prediction benchmarks show that our DenseVLM outperforms previous methods and exhibits promising scalability.

2. Related work

Open-vocabulary dense prediction. Open-vocabulary dense prediction approaches aim to overcome the constraints of predefined categories, thereby enhancing their application in object detection [13, 21, 36, 54] and image segmentation [11, 26, 27, 49, 50]. The recent success of pre-trained vision-language models, particularly CLIP [39], which exhibit impressive alignment between images and language, has further inspired advancements in this area. In open-vocabulary detection, recent studies [13, 45] exploit the zero-shot classification capabilities of CLIP models to effectively identify novel objects. Furthermore, several works [21, 47] construct object detectors that utilize frozen CLIP encoders, thereby reducing computational overhead while maintaining performance. For open-vocabulary segmentation, a common two-stage pipeline [6, 7, 32, 49] integrates a class-agnostic mask generator with a fixed CLIP encoder to achieve cross-modal alignment and mask classification. Recent methods also investigate the use of shared frozen CLIP with side adapter networks [51] or the adop-

tion of single-stage frameworks [53]. However, due to its training on image-text pairs, CLIP lacks precise local vision-language alignment, essential for dense prediction tasks. Although recent studies fine-tune CLIP for pixel-level [4, 48] or mask-level [18] alignment, they are constrained by the scarcity of densely labeled data.

Vision-language alignment at image and region levels. Pre-training visual-language models enable alignment between image and text representations [16, 35, 39]. By using image-text pairs [40] as training data, methods such as CLIP [39] and ALIGN [16] exhibit impressive zero-shot classification capabilities. To improve the alignment of vision-language of dense features, some train-free studies [22, 23, 43] attempt to modify the output layers of CLIP. Alternatively, recent weakly-supervised approaches [38] indirectly align visual patches and image-level language representations. Nevertheless, these methods generally yield unsatisfactory results.

For precise local region alignment, researchers utilize annotations from visual grounding datasets [30] to train models on region-text alignment. For example, some methods such as GLIP [25, 56] and Grounding DINO [30] learn region-language grounding from region-text pairs or generates pseudo region-text pairs like RegionCLIP [57]. In the context of open-vocabulary detection and segmentation, some works achieve dense visual and text alignment by using mask attention [7, 19, 50, 60] or fine-tuning CLIP [4, 17, 48]. However, these methods face scalability challenges in diverse open-world environments due to limitations in data annotation. To address the issue of annotated data scarcity, recent self-supervised methods like CLIPSelf [46] use cropped images for semantic alignment, while MaskEmbed [5] leverages masked patch embeddings for feature reconstruction. Despite these advances, the efficacy of self-distillation methods is constrained by the sub-optimal performance of the teacher model and is further compromised by foreground bias.

To overcome these limitations, we propose DenseVLM to learn unbiased region-language alignment from more powerful VLM representations. Unlike recent prompt learning approaches [42, 44, 52] that improve zero-shot classification performance via knowledge distillation, our DenseVLM focuses specifically on learning accurate region-language alignment.

3. Method

Our aim is to develop a region-language alignment model that effectively aligns local visual and semantic features, thereby enhancing the performance of VLMs in open-vocabulary dense prediction tasks. To achieve this, it is crucial to alleviate the foreground bias problem prevalent in previous VLMs [39, 41] that arises from training on image-

text pairs. Moreover, our approach seeks to receive better performance beyond the constraints of self-distillation [46].

3.1. VLM’s representation

VLMs are typically designed to learn both global visual and textual representations within a shared semantic space. In ViT-based VLMs [3, 41], dense visual features are extracted through residual attention blocks. Following [46, 60], we derive the dense feature map \mathcal{F} by modifying the final residual attention block, *i.e.*, removing the SoftMax operation and incorporating mapping layers. For a set of category labels $\{c^1, \dots, c^D\}$, where D is the total number of categories, textual descriptions are generated using a prompt-template strategy [13], yielding prompts like “*This a photo of the c in the scene.*” These prompts are then encoded into text embeddings $\mathcal{T} = \{\mathcal{T}^1, \dots, \mathcal{T}^D\}$ by the text encoder.

3.2. DenseVLM framework

We propose DenseVLM, an end-to-end region-language alignment framework designed to mitigate the challenge of foreground bias. DenseVLM achieves this by precisely aligning unlabeled regions with their corresponding categories. As shown in Fig. 3, the framework consists of two key stages. First, it retrieves category semantics for region features using the powerful VLMs (P-VLM) with frozen weights. Second, it decouples these region-language alignments into foreground and background for training VLMs (L-VLM). In particular, DenseVLM operates without requiring any annotations, but is based solely on categories of semantic diversity derived from large-scale datasets.

Image patches to semantic regions. To achieve region alignment, the patch-level visual features from Sec. 3.1 need to be transformed into semantic region features. We adopt a strategy similar to [46], dividing the dense feature map into an $m \times n$ grid of patches. Unlike this approach, we refrain from directly segmenting the input image, thereby enhancing both computational efficiency and representation effectiveness. In each training iteration, m and n are randomly selected from the set $\{2, \dots, M\}$, where M defaults to 6, allowing for varying patch grid sizes. The semantic region representation $\{\mathcal{F}^1, \dots, \mathcal{F}^{m \times n}\}$ is then extracted from dense feature map \mathcal{F} via pooling (RoIAlign) [15]. This patch sampling strategy effectively captures region features of both foreground objects and background scenes. However, due to the foreground bias in VLMs [39, 41, 46], we observe that background regions are usually misclassified as foreground classes, despite containing only a small proportion of foreground-related patches.

Powerful VLM for retrieval regions. Building on the dense representation extraction from VLM described in Sec. 3.1 and its ability to map image patches to semantic regions, the powerful VLM enables the extraction of both

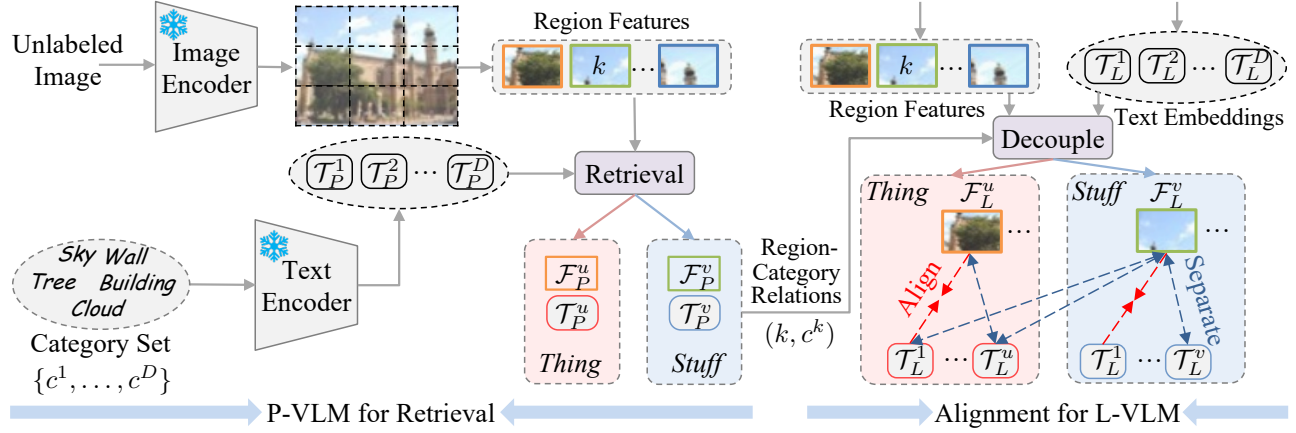


Figure 3. Overview of DenseVLM. For clarity, this diagram omits the dense visual and text features extracted by the training VLM (L-VLM), which are similar to those extracted by the powerful VLM (P-VLM). DenseVLM leverages the powerful VLM to **retrieve** categories for unlabeled regions and distinguish between foreground and background. During VLM training, DenseVLM **decouples** interference between features of foreground and background regions, **aligning** each region with its corresponding text embeddings.

region features $\mathcal{F}_P = \{\mathcal{F}_P^1, \dots, \mathcal{F}_P^{m \times n}\}$ and text embeddings $\mathcal{T}_P = \{\mathcal{T}_P^1, \dots, \mathcal{T}_P^D\}$. To broaden semantic diversity and coverage of region retrieval, we select categories from extensive datasets, specifically the COCO-Stuff [1] (171 categories) and the ADE20K [59] (847 categories) datasets, which cover a wide range of indoor and outdoor scenes. These categories are manually classified into two sets: foreground objects *Thing* (\mathcal{U}) and background regions *Stuff* (\mathcal{V}), which supports the subsequent decoupled alignment process. Next, unlabeled regions are retrieved and matched with the most relevant categories by computing the cosine similarity between the region features \mathcal{F}_P and text embeddings \mathcal{T}_P . For a specific region k , the cosine similarity between its features $\mathcal{F}_P^k = \mathcal{F}_P[k, :]$ and text embeddings of all categories is computed as:

$$\cos(\mathcal{F}_P^k, \mathcal{T}_P^i) = \frac{\mathcal{F}_P^k \cdot \mathcal{T}_P^i}{\|\mathcal{F}_P^k\| \|\mathcal{T}_P^i\|}, \quad \forall i = 1, 2, \dots, D \quad (1)$$

where \cdot denotes the dot product and $\|\cdot\|$ represents the Euclidean norm. The probability of associating this region with the categories is determined as follows:

$$p^k(y = c | \mathcal{F}_P^k, \mathcal{T}_P) = \frac{\exp(\cos(\mathcal{F}_P^k, \mathcal{T}_P^c) / \tau)}{\sum_{j=1}^D \exp(\cos(\mathcal{F}_P^k, \mathcal{T}_P^j) / \tau)}, \quad (2)$$

where $\tau = 0.01$ is a temperature hyperparameter.

The use of random grids to extract region features often introduces uncertainty in fully covering a single object, especially in scenarios with multiple objects. This uncertainty significantly affects the precision of the region-category alignment. To mitigate this issue, we leverage a region denoising scheme by discarding any region whose matching probability falls below a threshold θ , which is set to 0.3 by default. Therefore, this retrieval and denoising

process yields a more precise and reliable alignment of regions with their corresponding categories. The optimal category for each region k , denoted as c^k , is determined by: $c^k = \operatorname{argmax}(p^k)$, where each region-category relation is represented as (k, c^k) . This alignment is fundamental for the subsequent decoupled alignment process.

Decoupled region alignment to train VLMs. Upon the established region-category relations, we perform alignment between the region and text representations to train the L-VLM. A straightforward approach would be to directly align region features and text embeddings of their corresponding categories while maximizing the separation of unrelated categories. However, since the L-VLM directly inherits from the P-VLM, our experimental results in Sec. 4.2 reveal that this method exacerbates foreground bias, leading to improved foreground detection but limited gains in background recognition.

To mitigate this issue, we propose a decoupled alignment strategy that separates the alignment process for foreground and background regions. Specifically, we denote the region features of the training L-VLM as \mathcal{F}_L , using the same partitioning grid as the P-VLM. The text embeddings are represented as \mathcal{T}_L . By leveraging the region-category relations (k, c^k) retrieved by the P-VLM, we establish a one-to-one mapping for the L-VLM to associate the region features and their corresponding category embeddings. To distinguish the semantic regions of foreground and background, we decouple these region-category relations into two distinct groups, following the predefined category sets: *Thing* \mathcal{U} and *Stuff* \mathcal{V} . This classification facilitates the focused enhancement of the model’s capacity to recognize background regions, by aligning region features and their corresponding text embeddings while maintaining selective separation from text embeddings associated with irrelevant categories.

VLMs Frozen & Training	Region Cropping	Alignment Strategy	GPU Memory (per card)	Time Overhead (per epoch)	Boxes		Masks-T		Masks-S	
					Top1	Top5	Top1	Top5	Top1	Top5
ViT-B/16 & ViT-B/16	Images	Features KD	4*37G	25min	69.1	88.2	66.7	83.4	41.7	75.2
ViT-L/14 & ViT-B/16	Images	Features KD	4*39G	37min	24.2	52.4	23.4	51.1	10.1	39.1
ViT-L/14 & ViT-B/16	Images	Logics KD	4*39G	55min	72.2	89.8	68.8	83.8	42.6	75.2
ViT-L/14 & ViT-B/16	Features	DenseVLM	4*39G	23min	73.4	90.5	71.0	84.8	45.6	77.8

Table 1. Results and comparisons of various frameworks, including target VLMs for aligning representations, region cropping of frozen VLMs, and optimization strategies for region-language alignment, with GPU memory efficiency and time overhead. All models are trained on four A40 GPUs, with each epoch containing 118k images.

The alignment process can be effectively achieved by maximizing the cosine similarity for the region features and the text embeddings. According to Eqn. (1), when $c^k \in \mathcal{V}$, the probability q^k for a specific region is calculated as:

$$q^k = \frac{\exp(\cos(\mathcal{F}_L^k, \mathcal{T}_L^c)/\tau)}{\sum_{j=1}^{\mathcal{U} \cup \mathcal{V}} \exp(\cos(\mathcal{F}_L^k, \mathcal{T}_L^j)/\tau)}. \quad (3)$$

Similarly, when $c^k \in \mathcal{U}$, the probability \tilde{q}^k is computed as:

$$\tilde{q}^k = \begin{cases} \frac{\exp(\cos(\mathcal{F}_L^k, \mathcal{T}_L^c)/\tau)}{\sum_{j=1}^{\mathcal{U}} \exp(\cos(\mathcal{F}_L^k, \mathcal{T}_L^j)/\tau)} & \text{if } c \in \mathcal{U}, \\ 0 & \text{otherwise.} \end{cases} \quad (4)$$

The optimization objective is to minimize the expected negative log-likelihood of both q^k and \tilde{q}^k , *i.e.*, to minimize: $\mathbb{E}[-\log q^k] + \mathbb{E}[-\log \tilde{q}^k]$. This approach effectively reduces interference between foreground and background features, thereby enhancing the model’s precision in associating regions with their corresponding categories.

End-to-end optimization. As in Eqn. (3) and Eqn. (4), we also compute p^k and \tilde{p}^k for P-VLM. The proposed method DenseVLM supports end-to-end training through KL-divergence optimization as follows.

$$\mathcal{L}^k = \begin{cases} \text{KL}(p^k || q^k) & \text{if } c^k \in \mathcal{U}, \\ \text{KL}(\tilde{p}^k || \tilde{q}^k) & \text{otherwise.} \end{cases} \quad (5)$$

The overall loss for each image is computed as $\mathcal{L} = \sum_k^{m' \times n'} \mathcal{L}^k$, where the sum is taken over all regions, excluding those removed by the region denoising scheme.

4. Experiments

4.1. Benchmarks

Experiment settings. To verify the effectiveness of the proposed DenseVLM, we perform experiments in dense prediction tasks on the COCO panoptic [29] val2017 split and ADE20K panoptic [58] val split. Following CLIPSelf [46], we evaluate box classification using pooled box features (**Boxes**) and mask classification with pooled mask features, distinguishing foreground objects (**Masks-T**) from background content (**Masks-S**). The results are reported in terms of Top-1 and Top-5 mean accuracy across all experiments.

Implementation details. We employ the ViT-L/14 model from CLIPSelf [46] as the powerful P-VLM and ViT-B/16 from EVA-CLIP [41] as the training L-VLM. To enhance computational efficiency, the powerful VLM are kept frozen, and only the image encoder of the L-VLM is trained with pre-extracted text embeddings. Considering the practical application of the downstream tasks and the trade-off between performance and efficiency, we resize the input images to a uniform resolution of 512×512 pixels. The models are trained for 6 epochs using the AdamW [34] optimizer with a weight decay of 0.1. The initial learning rate is set to 1×10^{-5} with a cosine decay [33] schedule.

4.2. Ablation study

In our ablation study, DenseVLM is trained on the unlabeled images from the COCO train2017 split using 4×A40 GPUs and evaluated on the val2017 split. The experiments in Sec. 4.2 utilize the ViT-B/16 model from EVA-CLIP [41] for its superior efficiency and capacity.

Framework design exploration. We conduct ablation studies to explore the impact of design choices in DenseVLM, including target VLMs for aligning representations, region cropping of frozen VLMs, and optimization strategies for region-language alignment with a focus on GPU memory usage, and time overhead. We use a self-distillation strategy from CLIPSelf [46] as the baseline. As shown in Tab. 1, directly replacing the teacher model with ViT-L/14 CLIP leads to a significant performance drop. This decline is attributed to the disruption of the original visual-language alignment, despite transforming visual semantics from ViT-L/14 to ViT-B/16 CLIP. To address this, we replace feature distillation with logits distillation, which improves performance but clearly reduces training efficiency due to repeated feature extraction from ViT-L/14 CLIP for cropped images. In contrast, the proposed DenseVLM employs a more efficient feature-cropping strategy and retrieval and decoupled alignment framework, achieving superior performance while reducing training time and maintaining low GPU memory usage.

Ablation study on decoupled alignment. Tab. 2 analyzes the effect of the decoupled alignment strategy on DenseVLM. The retrieved category c^k can be categorized into

P-Thing		P-Stuff		Boxes	Masks-T	Masks-S
Thing	Stuff	Thing	Stuff			
✓	✓	✓	✓	74.3	70.9	42.6
✓	✗	✗	✓	74.2	70.8	42.0
✓	✓	✗	✓	74.1	71.0	41.3
✓	✗	✓	✓	73.4	70.9	45.6

Table 2. Ablation study on decoupled alignment. ✓ denotes that a region is separated from the categories in this set.

Categories	Boxes		Masks-T		Masks-S	
	Top1	Top5	Top1	Top5	Top1	Top5
133 (80)	71.1	88.5	68.7	83.0	44.7	75.2
171 (80)	72.3	89.8	69.4	85.8	44.2	76.0
273 (160)	72.3	89.9	70.1	84.4	44.9	76.4
316 (204)	73.4	90.5	71.0	84.8	45.6	77.8

Table 3. Ablation study on different category sets. The numbers in parentheses denote the number of foreground thing classes.

Thing and *Stuff*, referred to as ‘P-Thing’ and ‘P-Stuff’, respectively. DenseVLM leverages c^k for regions to selectively separate irrelevant *Thing* and *Stuff* categories. When regions do not align with all irrelevant categories, the model can better identify the foreground regions but struggles with distinguishing the background (1st row). In the fully decoupled setting, where each region separates only its corresponding irrelevant categories, performance further degrades (2nd row). The most pronounced foreground bias occurs when P-Thing suppresses *Stuff* but P-Stuff does not separate *Thing* (3rd row). In DenseVLM, we adopt a balanced strategy where P-Stuff separates both *Thing* and *Stuff*, while P-Thing does not separate *Stuff*, resulting in improved overall performance by mitigating bias (4th row).

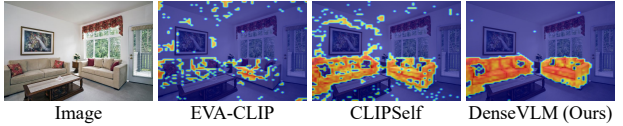
Ablation study on different category sets. Tab. 3 presents the effects of different category sets used for retrieval and alignment performance. We observe that as the number of categories increases, performance consistently improves. Adding only the background category helps the model distinguish foreground differences, as seen in rows 1 and 2, while incorporating more foreground categories leads to performance gains, as seen in rows 3 and 4. These improvements can be attributed to the enhanced representational capacity afforded by a broader category set.

Ablation study on the threshold θ . We also perform an ablation experiment to assess the impact of varying threshold θ values of region denoising, as introduced in Sec. 3.2. As shown in Tab. 4, the model performs the worst when θ is set to 0. When θ is set lower, the Top-5 accuracy increases, but the overall performance remains suboptimal. This may be due to low-confidence categories causing alignment confusion for the model. Conversely, setting θ too high filters out a significant portion of local images, decreasing per-

θ	Boxes		Masks-T		Masks-S	
	Top1	Top5	Top1	Top5	Top1	Top5
0.0	72.1	89.6	68.2	84.3	43.6	76.1
0.1	72.7	90.2	69.1	84.3	44.6	77.2
0.2	73.1	90.4	69.7	84.6	45.1	77.7
0.3	73.4	90.5	71.0	84.8	45.6	77.8
0.4	73.2	90.2	70.2	84.3	45.2	77.5
0.5	73.1	90.0	70.0	84.3	45.0	77.1
0.6	73.1	89.9	69.6	84.0	44.6	76.3

Table 4. Ablation study on threshold of θ in region denoising.

Text: “*This a photo of the sofa in the scene.*”



Text: “*This a photo of the tree in the scene.*”

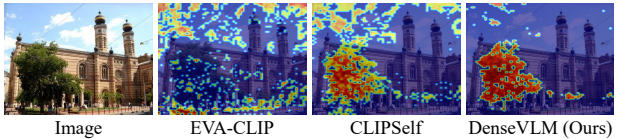


Figure 4. Comparing the alignment effect of our DenseVLM with other methods through visualizations of cosine similarity maps between visual features and text embeddings.

formance. To balance accuracy and efficiency, we select $\theta = 0.3$ for DenseVLM.

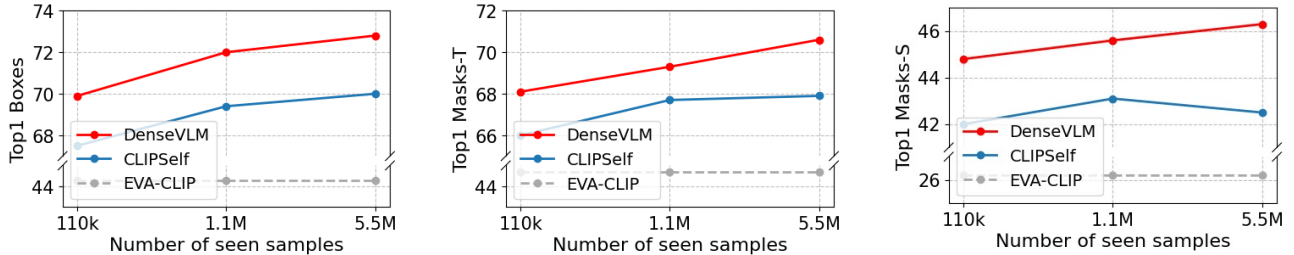
4.3. Comparison with other VLMs

Quantitative evaluation. We perform a comprehensive quantitative evaluation of dense representations across multiple VLMs on the COCO Panoptic [29] and ADE20K Panoptic [58] datasets. Specifically, we compare methods that are trained on large-scale image-text pairs, including OpenCLIP [3], DFN [10], SigLIP [55], and EVA-CLIP [41]. As shown in Tab. 5, while these methods achieve strong zero-shot image classification performance, their performance in region recognition is notably suboptimal. For instance, EVA-CLIP achieves only a Top-1 box classification accuracy of 44.3% on COCO and 33.0% on ADE20K. Although RegionCLIP [57], which is trained on region-text pairs, shows improved performance on COCO, but fails to generalize to datasets such as ADE20K. Moreover, CLIPSelf [46], which incorporates self-distillation, achieves higher box classification accuracy but performs poorly in mask classification. In contrast, our method, DenseVLM, notably outperforms these models, achieving a 4.3% improvement in Top-1 Mask-T accuracy and a 3.9% improvement in Top-1 Mask-S accuracy on COCO, highlighting its effectiveness in dense prediction tasks.

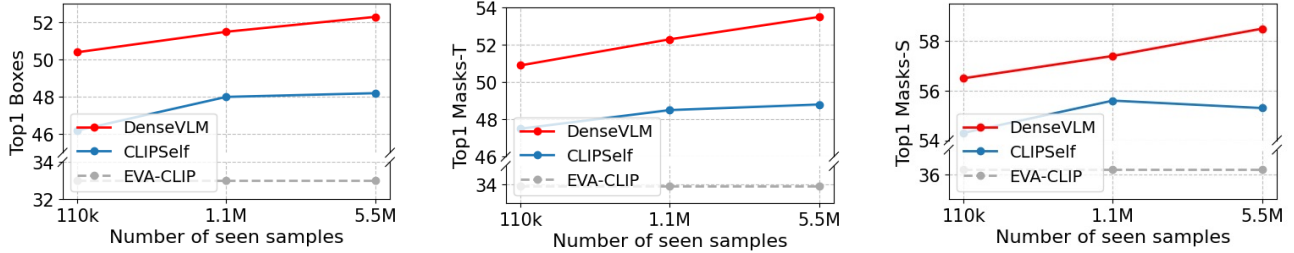
Qualitative results. We also visualize the attention maps

Method	COCO						ADE20K					
	Boxes		Masks-T		Masks-S		Boxes		Masks-T		Masks-S	
	Top1	Top5										
OpenCLIP [3]	49.8	74.3	51.9	72.2	29.2	54.9	28.4	54.1	29.6	53.4	37.9	66.6
DFN [10]	38.3	65.0	31.0	57.0	26.4	54.9	30.6	57.9	24.2	49.9	32.2	57.7
SigLIP [55]	39.9	61.4	40.4	60.1	30.3	56.4	25.9	49.2	27.3	47.6	34.5	57.3
EVA-CLIP [41]	44.3	68.7	44.7	66.0	26.2	51.9	33.0	57.6	33.9	56.2	36.2	62.3
RegionCLIP [†] [57]	68.5	89.5	60.7	84.3	22.0	53.5	43.2	72.2	34.0	62.6	37.7	68.6
CLIPSelf [†] [46]	69.1	88.2	66.7	83.0	41.7	75.2	48.1	77.7	47.5	74.2	53.7	82.8
DenseVLM [†] (Ours)	73.4	90.5	71.0	84.8	45.6	77.8	51.3	82.2	52.1	78.0	57.8	85.5

Table 5. Comparisons of different models on dense representation. We report the Top1 and Top5 mean accuracy on classifying boxes and panoptic masks (thing and stuff). [†] denotes models trained on the COCO and evaluated in a zero-shot setting on the ADE20K dataset.



(a) Top1 mean accuracy of models on COCO dense prediction benchmark.



(b) Top1 mean accuracy of models on ADE20K dense prediction benchmark.

Figure 5. Zero-shot comparisons of models pre-trained on datasets with three different scales. We select three training sets from the SA-1B dataset [20]: 100K, 1.1M, and 5.5M seen samples and perform the zero-shot evaluation on the COCO and ADE20K benchmarks.

generated by various methods in response to text descriptions of object categories by employing cosine similarity. As illustrated in Fig. 4, our DenseVLM exhibits superior accuracy and completeness in object localization compared to EVA-CLIP and CLIPSelf. Furthermore, DenseVLM is less affected by interference from other objects, effectively maintaining semantic separation, even when their visual features are fused within the network.

4.4. Zero-shot comparisons at different data scales

To investigate the effect of data scale on VLM performance, we select three training sets of varying sizes from the SA-1B [20] dataset: 100K, 1.1M, and 5.5M seen samples. We train our approach and the competing approach CLIPSelf on these subsets using 8×A40 GPUs and batch size of 48 per GPU. The resulting accuracy lines, presented in Fig. 5, reflect the performance of each model on the COCO and ADE20K benchmarks for open-vocabulary

dense prediction tasks. As the size of the training set increases, the performance improvement of CLIPSelf slows down, while DenseVLM continues to show consistent improvement, demonstrating its promising scalability. The ability of our DenseVLM to rely on unlabeled data enables it to scale effectively to larger datasets.

4.5. Extending to different backbones

To demonstrate the generality of our method, we extend it to several backbones, including ViT-B/16, R50x4, and ConvNeXt-B from OpenCLIP [3], as well as ViT-B/16 from EVA-CLIP [41]. From Tab. 6, we observe that CLIPSelf [46] is more effective with ViT-based architectures but is less effective with CNN-based architectures, particularly showing degraded performance with R50x4 compared to the baseline. In contrast, our approach yields consistent performance gains across all architectures, thereby broadening its applicability and potential. Furthermore, DenseVLM

Backbones	VLMs	Boxes	Masks-T	Masks-S
ViT-L/14	CLIPSelf	75.2	73.1	44.5
ViT-B/16	OpenCLIP	49.8	51.9	29.2
ViT-B/16	CLIPSelf	67.6	64.4	44.5
ViT-B/16	DenseVLM	71.9	70.0	47.8
ViT-B/16*	EVA-CLIP	44.3	44.7	26.2
ViT-B/16*	CLIPSelf	69.1	66.7	41.7
ViT-B/16*	DenseVLM	73.4	71.0	45.6
R50x4	OpenCLIP	59.2	50.5	39.1
R50x4	CLIPSelf	59.1	49.9	37.2
R50x4	DenseVLM	65.6	55.2	40.9
ConvNeXt-B	OpenCLIP	57.5	48.0	31.1
ConvNeXt-B	CLIPSelf	62.6	57.6	41.6
ConvNeXt-B	DenseVLM	67.1	63.4	43.5

Table 6. Results and comparisons of different backbones. * indicates the model initialized by EVA-CLIP [41].

Method	Backbone	A-150	A-847	PC-459
PACL [38]	ViT-B/16	31.4	-	-
OVSeg [27]	ViT-B/16	24.8	7.1	11.0
MAFT [17]	ConvNeXt-B	29.1	10.1	12.6
SED [48]	ConvNeXt-B	31.6	11.4	18.6
SCAN [31]	ViT-B/16	30.8	10.8	13.2
SAN [50]	ViT-B/16	27.4	10.0	13.0
SAN+DenseVLM	ViT-B/16	29.5_{+2.1}	10.4_{+0.4}	15.6_{+2.6}
CAT-Seg [4]	ViT-B/16	31.4	11.7	18.4
CAT-Seg+DenseVLM	ViT-B/16	34.1_{+2.1}	12.1_{+0.4}	18.7_{+0.3}

Table 7. Results on open-vocabulary semantic segmentation.

narrow the performance gap between powerful models like ViT-L/14 fine-tuned by CLIPSelf and lightweight models, with some lightweight models even outperforming the more powerful ones on the Masks-S metric.

4.6. Application to open-vocabulary dense tasks

Experiment settings. To evaluate the performance of the proposed DenseVLM in downstream tasks, we use DenseVLM as the backbone for open-vocabulary dense prediction tasks, including object detection and segmentation. To ensure fairness, our DenseVLM models are trained on the COCO train2017 split with an input resolution of 512×512 .

Open-vocabulary semantic segmentation. We apply DenseVLM models initialized with OpenAI CLIP [39] to open-vocabulary semantic segmentation, including SAN [50] with a frozen backbone and Cat-Seg [4] with a fine-tuned backbone. The models are trained on COCO-Stuff [1] and evaluated on the ADE20K [59] (ADE-150 and ADE-847) and PASCAL Context [37] (PC-459) datasets, using the mean Intersection-over-Union (mIoU) metric. As shown in Tab. 7, DenseVLM consistently improves performance across all evaluation datasets, further enhancing the state-of-the-art performance.

(a) OV-COCO benchmark				
Method	Backbone	AP ₅₀ ^{novel}	AP ₅₀ ^{base}	AP ₅₀
VLDet [28]	RN50	32.0	50.6	45.8
F-VLM [21]	RN50	28.0	-	39.6
BARON-Cap [45]	RN50	33.1	54.8	49.1
CORA [47]	RN50	35.1	35.5	35.4
RO-ViT [19]	ViT-B/16	30.2	-	41.5
RO-ViT [19]	ViT-L/16	33.0	-	47.7
F-ViT [46]	ViT-B/16	17.5	41.0	34.9
F-ViT+DenseVLM	ViT-B/16	33.1_{+15.6}	52.5_{+11.5}	47.4_{+12.5}

(b) OV-LVIS benchmark				
Method	Backbone	mAP _r	mAP _c	mAP
VLDet [28]	RN50	21.7	29.8	30.1
BARON-Cap [45]	RN50	22.6	27.6	27.6
F-VLM [21]	RN50	18.6	-	24.2
COR [47]	RN50x4	22.2	-	-
RO-ViT [19]	ViT-B/16	28.0	-	30.2
F-ViT [46]	ViT-B/16	11.5	12.3	15.4
F-ViT+DenseVLM	ViT-B/16	23.9_{+12.4}	18.4_{+6.1}	21.4_{+6.0}

Table 8. Results on open-vocabulary object detection.

Open-vocabulary object detection. Building on previous work [46], we construct open-vocabulary object detectors using the F-ViT architecture, a two-stage detector built on frozen ViTs from EVA-CLIP [41]. To balance efficiency and performance, we use an input resolution of 512×512 , as larger resolutions offer performance gains at the cost of efficiency. As shown in Tab. 8, we evaluate performance on the OV-COCO [2] benchmark by reporting box AP at IoU 0.5 for base, novel, and overall categories (AP₅₀^{novel}, AP₅₀^{base}, AP₅₀), and on OV-LVIS [14] benchmark by mean AP for rare (mAP_r), common (mAP_c), and all categories (mAP). Replacing the frozen EVA-CLIP ViTs with DenseVLM models leads to clear performance improvements on both benchmarks, achieving competitive performance relative to previous methods.

5. Conclusions

In this paper, we present DenseVLM, a framework designed to mitigate foreground bias in region-level vision-language alignment. DenseVLM can be seamlessly applied to open-vocabulary object detection and image segmentation tasks, demonstrating consistently clear performance improvements over the baseline models. Furthermore, we validate DenseVLM’s promising scaling ability by exploring efficient region retrieval and decoupled alignment, successfully implementing DenseVLM to the training data from the SA-1B dataset. Overall, DenseVLM offers a generalizable solution for improving dense representations in vision-language models across various backbones, which is essential for open-vocabulary dense prediction tasks.

DenseVLM: A Retrieval and Decoupled Alignment Framework for Open-Vocabulary Dense Prediction

Supplementary Material

We provide an overview of the supplementary materials to ensure a clear and comprehensive understanding.

- In Sec. A, we detail the limitations and broader impact of DenseVLM.
- In Sec. B, we present the training details.
- In Sec. C, we offer supplementary experiments on input image sizes, region proposals, backbones and category sets for training VLMs.
- In Sec. D, we show visualizations, including confusion matrices and cropping features predictions, to demonstrate foreground bias.
- In Sec. E, we present the dataset information for training and evaluation.

A. Limitations and broader impact

Limitations: Our aim is to develop a region-language alignment model that effectively integrates local visual and semantic features, thereby improving open-vocabulary dense prediction performance. Compared to previous pre-trained Vision-Language Models (VLMs) [3, 41, 46, 57], our proposed DenseVLM achieves superior results and significantly improves downstream task performance. We believe DenseVLM has even greater potential. 1) Scalability. DenseVLM is designed within an efficient, unsupervised region-language alignment framework, making it adaptable to various datasets. However, computational resource limitations have restricted our ability to scale to larger datasets. 2) Model capacity. We employ the ViT-L/14 model from CLIPSelf [46] as a powerful Pre-trained VLM (P-VLM). Utilizing more robust VLMs can yield better performance, and transferring their rich semantic knowledge to lightweight models is a promising direction. 3) Fine-grained Semantic. We categorize objects into broad *thing* and *stuff* classes. Fine-grained semantic segmentation and decoupled alignment would enhance the model’s ability to distinguish between similar categories. We plan to explore these avenues in our future research.

Broader impact: DenseVLM exhibits notable potential for open-vocabulary dense predictions within scenes, which can enhance various applications such as robotics and environmental monitoring. By enabling systems to recognize and interpret a wide range of objects and contexts without prior training on specific categories, DenseVLM facilitates more adaptive and versatile applications. Given its broad applicability and non-specialized nature, our method is designed to support a variety of technical advancements without directly addressing specific societal challenges.

item	value
image size	512 × 512
optimizer	AdamW [34]
learning rate	0.0001
β_1	0.9
β_2	0.98
weight decay	0.1
batch size (per card)	48
warmup steps [12]	1000
epochs	6
learning rate scheduler	cosine decay [33]
number of GPUs	4
automatic mixed precision ¹	True

Table 9. Training details of DenseVLM.

B. Training details

We train all models on NVIDIA A40 GPUs to ensure a fair comparison across experiments. The detailed configuration is provided in Table 9. For the SA-1B dataset [20], we use 8×A40 GPUs to ensure efficient and scalable training.

For open-vocabulary segmentation, we train the models such as SAN [50] and CAT-Seg [4] on the COCO-Stuff [1] dataset for 80k iterations. For open-vocabulary detection, models are trained for 3 epochs on the OV-COCO [2] benchmark and 48 epochs on OV-LVIS [14] benchmark.

C. Additional experiments

Ablation study on input image sizes. To evaluate the effect of input image size on DenseVLM, we conduct experiments with five distinct resolutions: 224, 320, 512, 768 and 1024 pixels, for both training and inference. As shown in Tab. 10, the model’s performance on the region classification task improves as the image resolution increases from 224 to 1024 pixels. This enhancement can be attributed to the greater detail captured at higher resolutions. However, this improvement comes at the cost of significantly increased GPU memory usage. However, this improvement comes at the cost of significantly increased GPU memory usage. Considering the trade-off between computational resources and model performance, we resize the images to

¹<https://developer.nvidia.com/automatic-mixed-precision>

Input Image Size	GPU Memory (per card)	COCO						ADE20K					
		Boxes		Masks-T		Masks-S		Boxes		Masks-T		Masks-S	
		Top1	Top5										
224	9G	60.1	79.9	49.4	62.4	35.3	64.2	40.0	70.0	36.3	56.4	50.3	77.0
320	11G	66.2	85.4	59.2	73.0	41.0	71.2	45.6	76.0	44.0	67.6	54.3	81.7
512	16G	73.4	90.5	71.0	84.8	45.6	77.8	51.3	82.2	52.1	78.0	57.8	85.5
768	27G	74.4	91.3	75.4	90.1	45.5	79.0	52.7	82.9	55.4	82.6	58.2	86.6
1024	39G	76.6	93.1	78.7	93.6	46.5	79.8	53.2	83.6	56.8	83.2	58.6	86.8

Table 10. Ablation study on input image sizes. We report the Top1 and Top5 mean accuracy on classifying boxes and panoptic masks on COCO panoptic and ADE20K panoptic benchmarks. The GPU memory usage corresponds to a batch size of 12 on A40 GPU.

Method	Region Proposals	COCO						ADE20K					
		Boxes		Masks-T		Masks-S		Boxes		Masks-T		Masks-S	
		Top1	Top5	Top1	Top5	Top1	Top5	Top1	Top5	Top1	Top5	Top1	Top5
CLIPSelf	✗	69.1	88.2	66.7	83.0	41.7	75.2	48.1	77.7	47.5	74.2	53.7	82.8
CLIPSelf	✓	70.2	89.2	68.1	83.5	35.7	71.8	49.8	79.7	51.5	76.0	50.9	80.7
DenseVLM	✗	73.4	90.5	71.0	84.8	45.6	77.8	51.3	82.2	52.1	78.0	57.8	85.5
DenseVLM	✓	74.4	91.3	75.4	90.1	45.9	79.0	52.7	82.9	55.4	82.6	58.2	86.6

Table 11. Ablation study on using region proposals. We report the Top1 and Top5 mean accuracy on classifying boxes and panoptic masks (thing and stuff) on COCO panoptic and ADE20K panoptic benchmarks.

512×512 pixels to achieve an optimal balance.

Ablation study on using region proposals. Following RegionCLIP [57] for fine-tuning VLMs with pseudo-labelled region-text pairs, we conduct a comparative analysis of our approach against CLIPSelf [46] in utilizing these pairs. As shown in Tab. 11, CLIPSelf employs the substitution of random image crops with pseudo region-text pairs, resulting in an enhanced recognition for foreground objects while concurrently observing a reduction in the accuracy of background identification. In contrast, our proposed DenseVLM achieves a notable improvement in the recognition accuracy of foreground objects while also improving the identification of background stuff.

Ablation study on various backbones. DenseVLM exhibits adaptability to diverse backbones. As shown in Tab. 12, our models achieve consistent superiority over prior approaches [3, 46] across all dense prediction tasks. Particularly, the ViT-B/16-based DenseVLM performs comparably to the ViT-L/14-based CLIPSelf [46]. Utilizing ViT-L/14 with a large number of parameters as initialization, DenseVLM achieves clearly enhancements across all evaluated metrics, thereby facilitating superior performance in dense prediction tasks.

Ablation study on different category sets. To assess the impact of varying category sets, we conduct experiments using four various sets: 133 (80), 171 (80), 273 (160), and 316 (160), categorized into foreground and background

classes. The set of 133 categories exclusively comprises COCO Panoptic [29] class set, while the 171-category set consists solely of COCO-Stuff [1] class set. The 273-category set integrates non-overlapping classes from both COCO-Stuff and the ADE20K Panoptic [58] dataset, which contains 150 categories. The 316-category set encompasses selected background classes from COCO-Stuff and the ADE20K dataset, which includes 847 categories. Our code accurately reflects all specified category sets.

As shown in Tab. 13, with the increase in the number of categories, the performance of our model progressively improves when evaluated on the COCO Panoptic and ADE20K Panoptic benchmarks. This is because the larger category sets provide a richer representation of objects and stuff, enabling the model to capture more fine-grained information, thereby enhancing its overall performance.

D. Visualizations

Confusion matrix. We compare the region classification results of our method against previous approaches through a confusion matrix visualization for panoptic masks (both thing and stuff categories) on the COCO Panoptic dataset. These confusion matrixs offer a systematic overview of region classification performance, illustrating the incidence of accurate and erroneous classifications, particularly facilitating a precise assessment of models’ accuracy in differentiating between thing and stuff categories. As shown in Fig. 6, Fig. 7, and Fig. 8, prior methods, including EVA-

backbones	VLMs	COCO						ADE20K					
		Boxes		Masks-T		Masks-S		Boxes		Masks-T		Masks-S	
		Top1	Top5	Top1	Top5	Top1	Top5	Top1	Top5	Top1	Top5	Top1	Top5
ViT-B/16	OpenCLIP	49.8	74.3	51.9	72.2	29.2	54.9	28.4	54.1	29.6	53.4	37.9	66.6
ViT-B/16	CLIPSelf	67.6	87.8	64.4	81.2	44.5	77.1	43.4	76.0	44.0	71.1	50.7	82.1
ViT-B/16	DenseVLM	71.9	90.2	70.0	84.3	47.8	79.4	48.5	79.2	49.0	75.2	55.1	85.2
ViT-B/16	DenseVLM*	73.4	90.5	71.0	84.8	45.6	77.8	51.3	82.2	52.1	78.0	57.8	85.5
ViT-L/14	OpenCLIP	21.2	45.3	26.6	48.9	11.2	27.2	48.1	11.9	34.1	13.9	11.1	32.4
ViT-L/14	CLIPSelf	68.3	90.1	67.1	84.5	37.7	71.3	47.1	77.5	47.7	74.4	48.9	82.3
ViT-L/14	DenseVLM	76.2	92.9	73.3	87.3	47.4	79.1	54.0	84.1	54.2	79.9	57.8	85.9
ViT-L/14	DenseVLM*	75.2	91.8	73.3	87.1	45.5	78.1	54.5	85.0	55.6	82.1	58.1	86.4

Table 12. Ablation study on various backbones. We report the Top1 and Top5 mean accuracy on classifying boxes and panoptic masks (thing and stuff) on COCO panoptic and ADE20K panoptic benchmarks. methodname* indicates the model initialized by EVA-CLIP [41].

Categories	COCO						ADE20K					
	Boxes		Masks-T		Masks-S		Boxes		Masks-T		Masks-S	
	Top1	Top5										
133 (80)	71.1	88.5	68.7	83.0	44.7	75.2	49.4	79.0	48.5	74.2	54.7	82.8
171 (80)	72.3	89.8	69.4	85.8	44.2	76.0	49.8	79.7	48.9	75.1	55.1	82.4
273 (160)	72.3	89.9	70.1	84.4	44.9	76.4	51.0	81.8	49.3	76.5	57.0	84.0
316 (204)	73.4	90.5	71.0	84.8	45.6	77.8	51.3	82.2	52.1	78.0	57.8	85.5

Table 13. Ablation study on different category sets. We report the Top1 and Top5 mean accuracy on classifying boxes and panoptic masks (thing and stuff) on COCO panoptic and ADE20K panoptic benchmarks.

CLIP [41], RegionCLIP [57], and CLIPSelf [46], often misclassify background regions as co-occurring foreground classes, such as incorrectly identifying *snow* as *skis* or *sky* as *kite*. In contrast, as demonstrated in Fig. 9, our DenseVLM achieves higher accuracy in recognizing each category, with a notable improvement in the precision of background object identification.

Image grid patches classification. We visualize the classification results of image grid patches using the powerful ViT-L/14 model from CLIPSelf [46]. As shown in Fig. 10, the model demonstrates a stronger focus on foreground object recognition, despite substantial portions of background patch regions being misclassified as foreground objects. The lightweight VLMs are prone to learning these errors. Furthermore, regions with incorrect classifications typically have low confidence scores, making it essential to filter out these regions.

E. Datasets of training and evaluation

COCO: COCO [29] is a large-scale panoptic segmentation dataset encompassing 80 *Thing* and 53 *Stuff* categories. The dataset comprises 118,000 images designated for the training set and 5,000 images for the validation set.

ADE20k: ADE20k [59] spans a broad spectrum of indoor and outdoor scenes, comprising 2,000 images for the validation set. This dataset includes 100 *Thing* and 50 *Stuff* cate-

gories. We evaluate open-vocabulary semantic annotations using both the extensive 847-category version (referred to as A-847) and the more frequently adopted 150-category version (referred to as A-150).

Pascal Context: Pascal-Context [9] constitutes an extensive dataset derived from Pascal-VOC 2010. We evaluate open-vocabulary semantic annotations using the complete set of 459 classes, referred to as PC-459.

OV-COCO: The open-vocabulary detection COCO (OV-COCO) benchmark, introduced in OV-RCNN [54], divides the 65 object categories in the COCO dataset into 48 base categories and 17 novel categories.

OV-LVIS: The open-vocabulary detection LVIS (OV-LVIS) benchmark, introduced in ViLD [13], defines the 337 rare categories from LVIS v1.0 dataset [14] as novel categories.

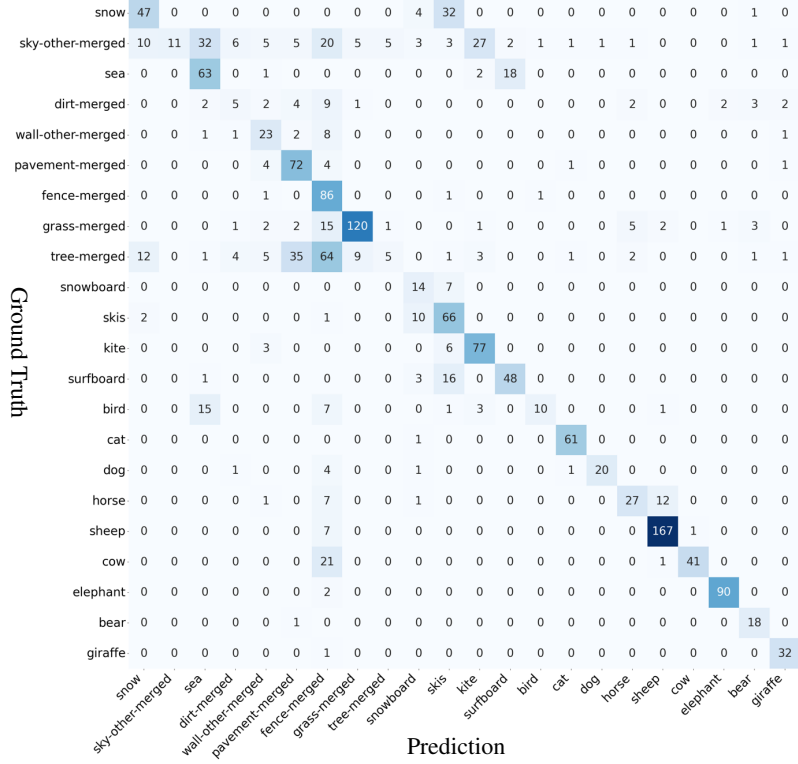


Figure 6. Confusion matrix visualization for region classification results of EVA-CLIP.

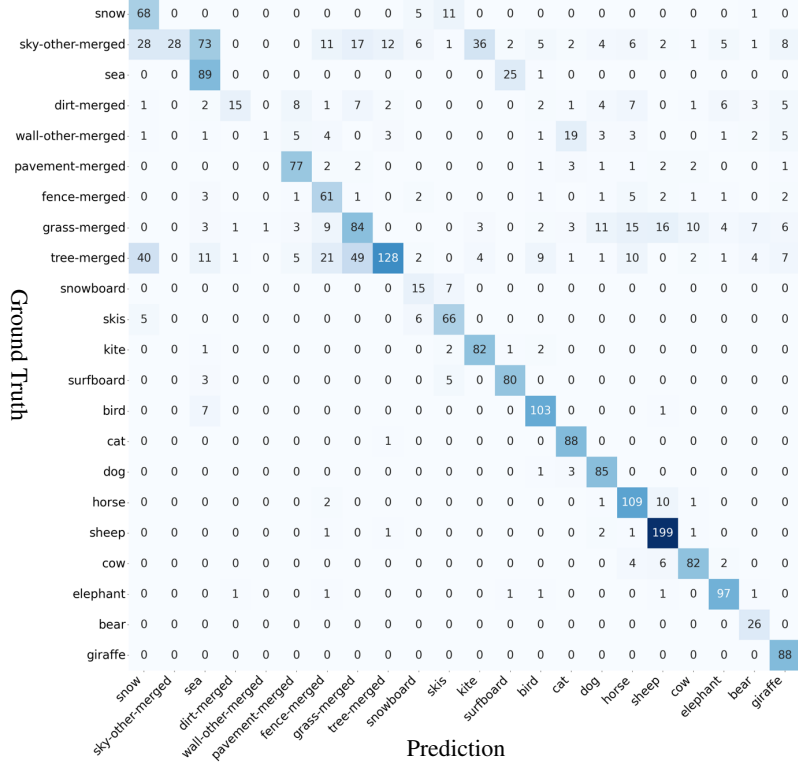


Figure 7. Confusion matrix visualization for region classification results of RegionCLIP.

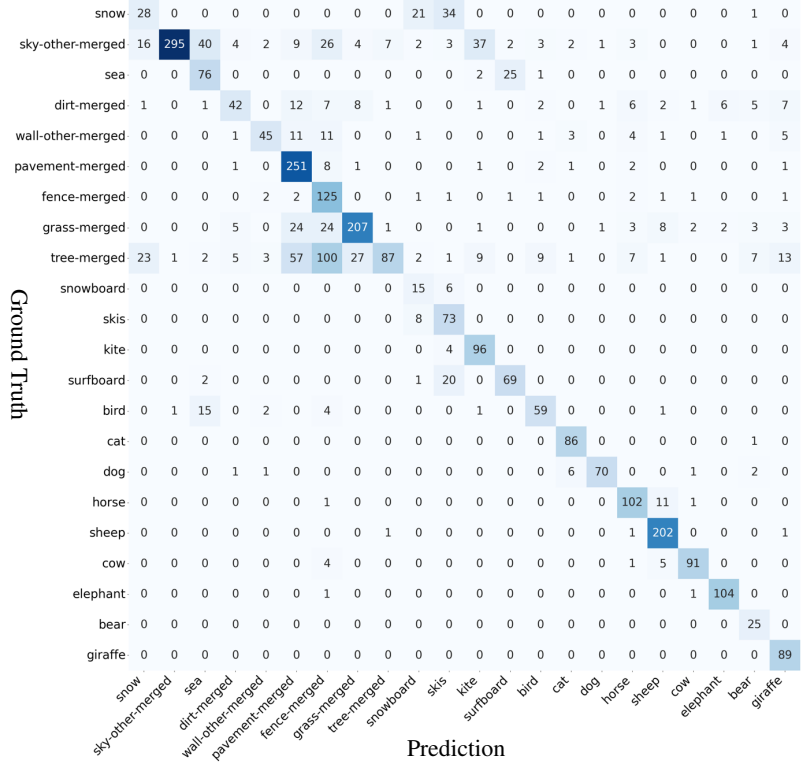


Figure 8. Confusion matrix visualization for region classification results of CLIPSelf.

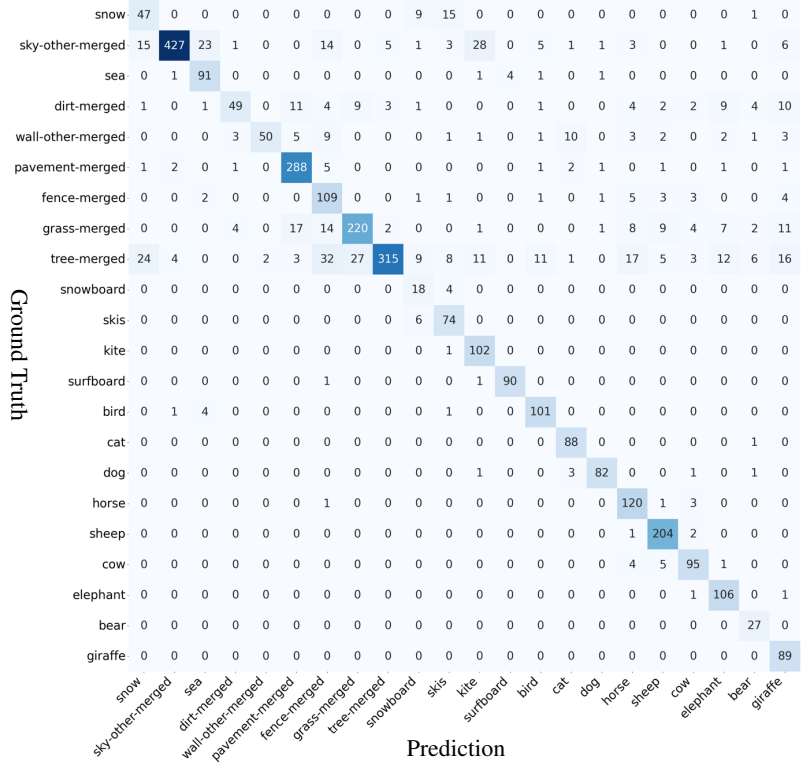


Figure 9. Confusion matrix visualization for region classification results of DenseVLM.

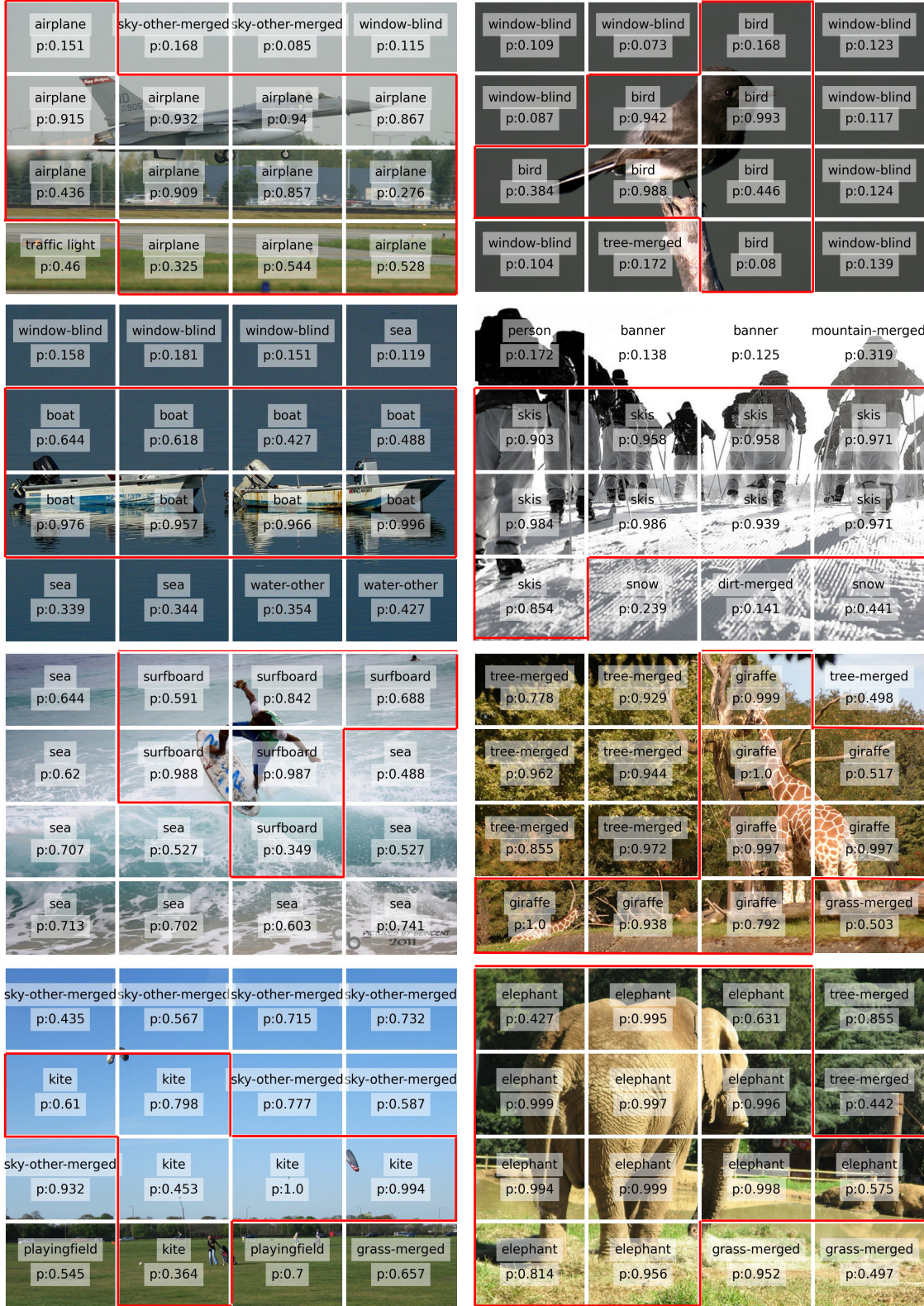


Figure 10. Visualization of image grid patches classification. The powerful ViT-L/14 model exhibits a pronounced focus on foreground object recognition, even when significant portions of background patches are misclassified as foreground objects.

References

[1] Holger Caesar, Jasper Uijlings, and Vittorio Ferrari. Coco-stuff: Thing and stuff classes in context. In *CVPR*, pages 1209–1218, 2018. [4](#), [8](#), [9](#), [10](#)

[2] Xinlei Chen, Hao Fang, Tsung-Yi Lin, Ramakrishna Vedantam, Saurabh Gupta, Piotr Dollár, and C Lawrence Zitnick. Microsoft coco captions: Data collection and evaluation server. *arXiv preprint arXiv:1504.00325*, 2015. [2](#), [8](#), [9](#)

[3] Mehdi Cherti, Romain Beaumont, Ross Wightman, Mitchell Wortsman, Gabriel Ilharco, Cade Gordon, Christoph Schuhmann, Ludwig Schmidt, and Jenia Jitsev. Reproducible scaling laws for contrastive language-image learning. In *CVPR*, pages 2818–2829, 2023. [3](#), [6](#), [7](#), [9](#), [10](#)

[4] Seokju Cho, Heeseong Shin, Sunghwan Hong, Anurag Arnab, Paul Hongsuck Seo, and Seungryong Kim. Cat-seg: Cost aggregation for open-vocabulary semantic segmentation. In *CVPR*, 2024. [1](#), [2](#), [3](#), [8](#), [9](#)

[5] Ian Covert, Tony Sun, James Zou, and Tatsunori Hashimoto. Locality alignment improves vision-language models. *arXiv preprint arXiv:2410.11087*, 2024. [1](#), [3](#)

[6] Jian Ding, Nan Xue, Gui-Song Xia, and Dengxin Dai. De-coupling zero-shot semantic segmentation. In *CVPR*, pages 11583–11592, 2022. [2](#)

[7] Zheng Ding, Jieke Wang, and Zhuowen Tu. Open-vocabulary panoptic segmentation with maskclip. *arXiv preprint arXiv:2208.08984*, 2022. [2](#), [3](#)

[8] Alexey Dosovitskiy. An image is worth 16x16 words: Transformers for image recognition at scale. *arXiv preprint arXiv:2010.11929*, 2020. [2](#)

[9] Mark Everingham, Luc Van Gool, Christopher KI Williams, John Winn, and Andrew Zisserman. The pascal visual object classes (voc) challenge. *IJCV*, 88:303–338, 2010. [11](#)

[10] Alex Fang, Albin Madappally Jose, Amit Jain, Ludwig Schmidt, Alexander Toshev, and Vaishaal Shankar. Data filtering networks. *arXiv preprint arXiv:2309.17425*, 2023. [6](#), [7](#)

[11] Golnaz Ghiasi, Xiuye Gu, Yin Cui, and Tsung-Yi Lin. Scaling open-vocabulary image segmentation with image-level labels. In *ECCV*, pages 540–557, 2022. [1](#), [2](#)

[12] Priya Goyal, Piotr Dollár, Ross Girshick, Pieter Noordhuis, Lukasz Wesolowski, Aapo Kyrola, Andrew Tulloch, Yangqing Jia, and Kaiming He. Accurate, large mini-batch sgd: Training imagenet in 1 hour. *arXiv preprint arXiv:1706.02677*, 2018. [9](#)

[13] Xiuye Gu, Tsung-Yi Lin, Weicheng Kuo, and Yin Cui. Open-vocabulary object detection via vision and language knowledge distillation. In *ICLR*, pages 1–20, 2022. [1](#), [2](#), [3](#), [11](#)

[14] Agrim Gupta, Piotr Dollar, and Ross Girshick. Lvis: A dataset for large vocabulary instance segmentation. In *CVPR*, 2019. [2](#), [8](#), [9](#), [11](#)

[15] Kaiming He, Georgia Gkioxari, Piotr Dollár, and Ross Girshick. Mask r-cnn. In *ICCV*, pages 2961–2969, 2017. [3](#)

[16] Chao Jia, Yinfai Yang, Ye Xia, Yi-Ting Chen, Zarana Parekh, Hieu Pham, Quoc Le, Yun-Hsuan Sung, Zhen Li, and Tom Duerig. Scaling up visual and vision-language representation learning with noisy text supervision. In *ICML*, pages 4904–4916, 2021. [3](#)

[17] Siyu Jiao, Yunchao Wei, Yaowei Wang, Yao Zhao, and Humphrey Shi. Learning mask-aware clip representations for zero-shot segmentation. *NeurIPS*, 36:35631–35653, 2023. [3](#), [8](#)

[18] Siyu Jiao, Hongguang Zhu, Jiannan Huang, Yao Zhao, Yunchao Wei, and Humphrey Shi. Collaborative vision-text representation optimizing for open-vocabulary segmentation. *arXiv preprint arXiv:2408.00744*, 2024. [3](#)

[19] Dahun Kim, Anelia Angelova, and Weicheng Kuo. Region-aware pretraining for open-vocabulary object detection with vision transformers. In *CVPR*, pages 11144–11154, 2023. [1](#), [3](#), [8](#)

[20] Alexander Kirillov, Eric Mintun, Nikhila Ravi, Hanzi Mao, Chloe Rolland, Laura Gustafson, Tete Xiao, Spencer Whitehead, Alexander C Berg, Wan-Yen Lo, et al. Segment anything. In *ICCV*, pages 4015–4026, 2023. [2](#), [7](#), [9](#)

[21] Weicheng Kuo, Yin Cui, Xiuye Gu, AJ Piergiovanni, and Anelia Angelova. F-vlm: Open-vocabulary object detection upon frozen vision and language models. In *ICLR*, 2022. [1](#), [2](#), [8](#)

[22] Mengcheng Lan, Chaofeng Chen, Yiping Ke, Xinjiang Wang, Litong Feng, and Wayne Zhang. Clearclip: Decomposing clip representations for dense vision-language inference. In *ECCV*, 2024. [3](#)

[23] Mengcheng Lan, Chaofeng Chen, Yiping Ke, Xinjiang Wang, Litong Feng, and Wayne Zhang. Proxycip: Proxy attention improves clip for open-vocabulary segmentation. In *ECCV*, 2024. [3](#)

[24] Yann LeCun, Bernhard Boser, John S Denker, Donnie Henderson, Richard E Howard, Wayne Hubbard, and Lawrence D Jackel. Backpropagation applied to handwritten zip code recognition. *Neural computation*, 1(4):541–551, 1989. [2](#)

[25] Liunian Harold Li, Pengchuan Zhang, Haotian Zhang, Jianwei Yang, Chunyuan Li, Yiwu Zhong, Lijuan Wang, Lu Yuan, Lei Zhang, Jenq-Neng Hwang, et al. Grounded language-image pre-training. In *CVPR*, pages 10965–10975, 2022. [1](#), [3](#)

[26] Yunheng Li, ZhongYu Li, Quansheng Zeng, Qibin Hou, and Ming-Ming Cheng. Cascade-clip: Cascaded vision-language embeddings alignment for zero-shot semantic segmentation. In *ICML*, pages 28243–28258, 2024. [1](#), [2](#)

[27] Feng Liang, Bichen Wu, Xiaoliang Dai, Kunpeng Li, Yinan Zhao, Hang Zhang, Peizhao Zhang, Peter Vajda, and Diana Marculescu. Open-vocabulary semantic segmentation with mask-adapted clip. In *CVPR*, pages 7061–7070, 2023. [1](#), [2](#), [8](#)

[28] Chuang Lin, Peize Sun, Yi Jiang, Ping Luo, Lizhen Qu, Ghollamreza Haffari, Zehuan Yuan, and Jianfei Cai. Learning object-language alignments for open-vocabulary object detection. In *ICLR*, 2023. [8](#)

[29] Tsung-Yi Lin, Michael Maire, Serge Belongie, James Hays, Pietro Perona, Deva Ramanan, Piotr Dollár, and C Lawrence Zitnick. Microsoft coco: Common objects in context. In *ECCV*, 2014. [5](#), [6](#), [10](#), [11](#)

[30] Shilong Liu, Zhaoyang Zeng, Tianhe Ren, Feng Li, Hao Zhang, Jie Yang, Chunyuan Li, Jianwei Yang, Hang Su, Jun Zhu, et al. Grounding dino: Marrying dino with grounded pre-training for open-set object detection. *arXiv preprint arXiv:2303.05499*, 2023. 1, 3

[31] Yong Liu, Sule Bai, Guanbin Li, Yitong Wang, and Yansong Tang. Open-vocabulary segmentation with semantic-assisted calibration. In *Proceedings of the IEEE/CVF Conference on Computer Vision and Pattern Recognition (CVPR)*, pages 3491–3500, 2024. 8

[32] Yong Liu, Sule Bai, Guanbin Li, Yitong Wang, and Yansong Tang. Open-vocabulary segmentation with semantic-assisted calibration. In *CVPR*, 2024. 2

[33] Ilya Loshchilov and Frank Hutter. SGDR: Stochastic gradient descent with warm restarts. In *ICLR*, 2017. 5, 9

[34] Ilya Loshchilov and Frank Hutter. Decoupled weight decay regularization. In *ICLR*, 2019. 5, 9

[35] Jiasen Lu, Dhruv Batra, Devi Parikh, and Stefan Lee. Vilbert: Pretraining task-agnostic visiolinguistic representations for vision-and-language tasks. *NeurIPS*, pages 13–23, 2019. 3

[36] Matthias Minderer, Alexey Gritsenko, Austin Stone, Maxim Neumann, Dirk Weissenborn, Alexey Dosovitskiy, Aravindh Mahendran, Anurag Arnab, Mostafa Dehghani, Zhuoran Shen, et al. Simple open-vocabulary object detection. In *ECCV*, pages 728–755, 2022. 1, 2

[37] Roozbeh Mottaghi, Xianjie Chen, Xiaobai Liu, Nam-Gyu Cho, Seong-Whan Lee, Sanja Fidler, Raquel Urtasun, and Alan Yuille. The role of context for object detection and semantic segmentation in the wild. In *CVPR*, pages 891–898, 2014. 8

[38] Jishnu Mukhoti, Tsung-Yu Lin, Omid Poursaeed, Rui Wang, Ashish Shah, Philip HS Torr, and Ser-Nam Lim. Open vocabulary semantic segmentation with patch aligned contrastive learning. In *CVPR*, pages 19413–19423, 2023. 3, 8

[39] Alec Radford, Jong Wook Kim, Chris Hallacy, Aditya Ramesh, Gabriel Goh, Sandhini Agarwal, Girish Sastry, Amanda Askell, Pamela Mishkin, Jack Clark, et al. Learning transferable visual models from natural language supervision. In *ICML*, pages 8748–8763, 2021. 1, 2, 3, 8

[40] Christoph Schuhmann, Romain Beaumont, Richard Vencu, Cade Gordon, Ross Wightman, Mehdi Cherti, Theo Coombes, Aarush Katta, Clayton Mullis, Mitchell Wortsman, et al. Laion-5b: An open large-scale dataset for training next generation image-text models. In *NeurIPS*, pages 25278–25294, 2022. 3

[41] Quan Sun, Yuxin Fang, Ledell Wu, Xinlong Wang, and Yue Cao. Eva-clip: Improved training techniques for clip at scale. *arXiv preprint arXiv:2303.15389*, 2023. 1, 2, 3, 5, 6, 7, 8, 9, 11

[42] Ximeng Sun, Pengchuan Zhang, Peizhao Zhang, Hardik Shah, Kate Saenko, and Xide Xia. Dime-fm : Distilling multimodal and efficient foundation models. In *ICCV*, pages 15521–15533, 2023. 3

[43] Feng Wang, Jieru Mei, and Alan Yuille. Sclip: Rethinking self-attention for dense vision-language inference. In *ECCV*, pages 315–332, 2025. 3

[44] Yixuan Wei, Han Hu, Zhenda Xie, Zheng Zhang, Yue Cao, Jianmin Bao, Dong Chen, and Baining Guo. Contrastive learning rivals masked image modeling in fine-tuning via feature distillation. *arXiv preprint arXiv:2205.14141*, 2022. 3

[45] Size Wu, Wenwei Zhang, Sheng Jin, Wentao Liu, and Chen Change Loy. Aligning bag of regions for open-vocabulary object detection. In *CVPR*, pages 15254–15264, 2023. 2, 8

[46] Size Wu, Wenwei Zhang, Lumin Xu, Sheng Jin, Xiangtai Li, Wentao Liu, and Chen Change Loy. Clipself: Vision transformer distills itself for open-vocabulary dense prediction. *ICLR*, 2024. 1, 2, 3, 5, 6, 7, 8, 9, 10, 11

[47] Xiaoshi Wu, Feng Zhu, Rui Zhao, and Hongsheng Li. Cora: Adapting clip for open-vocabulary detection with region prompting and anchor pre-matching. In *CVPR*, pages 7031–7040, 2023. 2, 8

[48] Bin Xie, Jiale Cao, Jin Xie, Fahad Shahbaz Khan, and Yanwei Pang. Sed: A simple encoder-decoder for open-vocabulary semantic segmentation. In *CVPR*, 2024. 3, 8

[49] Jiarui Xu, Sifei Liu, Arash Vahdat, Wonmin Byeon, Xiaolong Wang, and Shalini De Mello. Open-vocabulary panoptic segmentation with text-to-image diffusion models. In *CVPR*, pages 2955–2966, 2023. 1, 2

[50] Mengde Xu, Zheng Zhang, Fangyun Wei, Han Hu, and Xiang Bai. Side adapter network for open-vocabulary semantic segmentation. In *CVPR*, pages 2945–2954, 2023. 1, 2, 3, 8, 9

[51] Mengde Xu, Zheng Zhang, Fangyun Wei, Han Hu, and Xiang Bai. San: Side adapter network for open-vocabulary semantic segmentation. *IEEE TPAMI*, pages 1–17, 2023. 2

[52] Chuanguang Yang, Zhulin An, Libo Huang, Junyu Bi, Xinqiang Yu, Han Yang, Boyu Diao, and Yongjun Xu. Clip-kd: An empirical study of clip model distillation. In *CVPR*, 2024. 3

[53] Qihang Yu, Ju He, Xueqing Deng, Xiaohui Shen, and Liang-Chieh Chen. Convolutions die hard: Open-vocabulary segmentation with single frozen convolutional clip. *NeurIPS*, 2023. 3

[54] Alireza Zareian, Kevin Dela Rosa, Derek Hao Hu, and Shih-Fu Chang. Open-vocabulary object detection using captions. In *CVPR*, pages 14393–14402, 2021. 1, 2, 11

[55] Xiaohua Zhai, Basil Mustafa, Alexander Kolesnikov, and Lucas Beyer. Sigmoid loss for language image pre-training. In *ICCV*, pages 11975–11986, 2023. 6, 7

[56] Haotian Zhang, Pengchuan Zhang, Xiaowei Hu, Yen-Chun Chen, Liunian Li, Xiyang Dai, Lijuan Wang, Lu Yuan, Jenq-Neng Hwang, and Jianfeng Gao. Glipv2: Unifying localization and vision-language understanding. *NeurIPS*, 35: 36067–36080, 2022. 1, 3

[57] Yiwu Zhong, Jianwei Yang, Pengchuan Zhang, Chunyuan Li, Noel Codella, Liunian Harold Li, Luwei Zhou, Xiyang Dai, Lu Yuan, Yin Li, et al. Regionclip: Region-based language-image pretraining. In *CVPR*, pages 16793–16803, 2022. 1, 2, 3, 6, 7, 9, 10, 11

[58] Bolei Zhou, Hang Zhao, Xavier Puig, Sanja Fidler, Adela Barriuso, and Antonio Torralba. Scene parsing through ade20k dataset. In *CVPR*, 2017. 5, 6, 10

- [59] Bolei Zhou, Hang Zhao, Xavier Puig, Tete Xiao, Sanja Fidler, Adela Barriuso, and Antonio Torralba. Semantic understanding of scenes through the ade20k dataset. *IJCV*, 127:302–321, 2019. [4](#), [8](#), [11](#)
- [60] Chong Zhou, Chen Change Loy, and Bo Dai. Extract free dense labels from clip. In *ECCV*, page 696–712, 2022. [1](#), [3](#)
- [61] Yuanbing Zhu, Bingke Zhu, Zhen Chen, Huan Xu, Ming Tang, and Jinqiao Wang. Mrovseg: Breaking the resolution curse of vision-language models in open-vocabulary semantic segmentation. *arXiv preprint arXiv:2408.14776*, 2024. [2](#)